# How two gravity-gradient inversion methods can be used to reveal different geologic features of ore deposit — A case study from the Quadrilátero Ferrífero (Brazil)

Dionísio U. Carlos [a,b,*], Leonardo Uieda [a], Valeria C.F. Barbosa [a]

[a] *Observatório Nacional, Departamento de Geofísica, Gal. José Cristino, 77, Rio de Janeiro, RJ 20921-400, Brazil*
[b] *Vale, Departamento de Exploração Mineral de Ferrosos, Avenida de Ligação, 3580, Nova Lima, MG, 34000-000, Brazil*

### ARTICLE INFO

### ABSTRACT

Airborne gravity gradiometry data have been recently used in mining surveys to map the 3D geometry of ore deposits. This task can be achieved by different gravity-gradient inversion methods, many of which use a voxel-based discretization of the Earth's subsurface. To produce a unique and stable solution, an inversion method introduces particular constraints. One constraining inversion introduces a depth-weighting function in the first-order Tikhonov regularization imposing a smoothing on the density-contrast distributions that are not restricted to near-surface regions. Another gravity-gradient inversion, the method of planting anomalous densities, imposes compactness and sharp boundaries on the density-contrast distributions. We used these two inversion methods to invert the airborne gravity-gradient data over the iron-ore deposit at the southern flank of the Gandarela syncline in Quadrilátero Ferrífero (Brazil). Because these methods differ from each other in the particular constraint used, the estimated 3D density-contrast distributions reveal different geologic features of ore deposit. The depth-weighting smoothing inversion reveals variable dip directions along the strike of the retrieved iron-ore body. The planting anomalous density inversion estimates a compact iron-ore mass with a single density contrast, which reveals a variable volume of the iron ore along its strike increasing towards the hinge zone of the Gandarela syncline which is the zone of maximum compression. The combination of the geologic features inferred from each estimate leads to a synergistic effect, revealing that the iron-ore deposit is strongly controlled by the Gandarela syncline.

© 2016 Elsevier B.V. All rights reserved.

## Contents

\* Corresponding author.
  *E-mail address:* dionisio.carlos@vale.com (D.U. Carlos).

## 1. Introduction

Different geologic models as possible mechanisms for formation of giant banded iron formations (BIF) have been proposed in the literature. According to McLellan et al. (2004), among these models two aspects of ore formation are commonly accepted: (1) ore genesis involved replacement of BIFs, and (2) ore bodies are spatially related to structural features, e.g. fault and folds. Understanding the relationship between the structural features and the geometry of the iron-ore deposit has significant importance (Dalstra, 2006). Hence, one of the challenges for the exploration industry has been the 3D visualization of the iron-ore geometry. The knowledge of the 3D geometry of the iron-ore mass aids the geologists in understanding the structural controls of bedded iron ore. The better understanding of structural features of the iron-ore mineralization can assist the geologist, for example, in designing the drill planning. One approach adopted by exploration geologists to delineate the 3D geometry of an iron-ore mineralization consists in creating 3D wireframes based on extensive drilling database geometry (Hagemann et al., 2007). An alternative is to predict the 3D geometry of an iron-ore mineralization by inverting the geophysical data.

The magnetic data can be used for studying ore deposits. However, in some areas the ore body can present remanent magnetization and (or) can be associated with low magnetization intensity. These facts makes difficult to use magnetic data to estimate ore bodies.

More recently, gravity-gradient data have been used either in oil exploration (e.g., Routh et al., 2001; Barnes and Barraud, 2012; Oliveira and Barbosa, 2013) or in mineral exploration (e.g., Dransfield et al., 2001; Lane and Peljo, 2004; Dransfield, 2007; Zhdanov et al., 2004; Uieda and Barbosa, 2012; Martinez et al., 2013). Specifically, the gravity-gradient inversion has been used as a tool in predicting the geometry of geologic bodies. The inversion of gravity-gradient data to predict the geometry of iron-ore mineralization can be done by estimating the density-contrast distribution in the Earth's subsurface. However, reconstructing a subsurface density-contrast distribution from gravity-gradient inversion has a nonunique solution; so, it admits infinite solutions (Silva et al., 2002). This nonuniqueness can be reduced if the set of feasible solutions is constrained by prior information about the sources (Barbosa et al., 2002). To estimate a meaningful geologic solution, the inverse methods introduce different types of prior knowledge about the iron-ore bodies so that geologically realistic density-contrast distribution, still fitting the gravity-gradient data, can be reconstructed. Mathematically, the a priori information about the sources is introduced in the inverse problem as constrained. Hence, different constraints on the anomalous mass distribution allow the introduction of different kinds of prior information about the geometry of the sources.

Usually, a single method is used to invert geophysical data. In this work, we inverted the airborne gravity-gradient data from the southern flank of the Gandarela syncline in Quadrilátero Ferrífero (Brazil) by using two constraining inversion methods. Our goal is to show that by applying two quite different gravity-gradient inversion methods their estimates can reveal different geologic characteristics that are not clearly seen by using only one method. This synergy is only achieved by using contrasting inversion methods.

The first method chosen is named the depth-weighting smoothing inversion (Li, 2001) which imposes a smoothing character on the solution. In this inversion method, the density-contrast distribution is constrained by a depth-weighting function aiming at estimating non-outcropping iron-ore bodies. The second one is named planting anomalous density inversion (Uieda and Barbosa, 2012) which imposes homogeneity and compactness on the solution. This inversion method allows just two possibilities for the density-contrast estimate: zero or a pre-specified nonnull value. Our results show that the smooth character imposed on the solution by the depth-weighting smoothing inversion reveals that the estimated iron body dips inwards towards the Gandarela syncline axis. On the other hand, the constraints imposed by the planting anomalous density inversion reveal a large volume over

the hinge zone of the Gandarela syncline. The synergistic effect of the estimates obtained by these quite different methods brings out that the iron-ore mineralization is controlled by the Gandarela syncline.

## 2. Methodology

Let $\mathbf{d^o}$ be an N-dimensional vector of gravity-gradient observations produced by anomalous density distribution within a 3D region of the subsurface. This region can be discretized into a mesh of 3D right-rectangular prisms juxtaposed in $x-$, $y-$, and $z-$ directions of a right-sided Cartesian coordinate system. We define this coordinate system with its
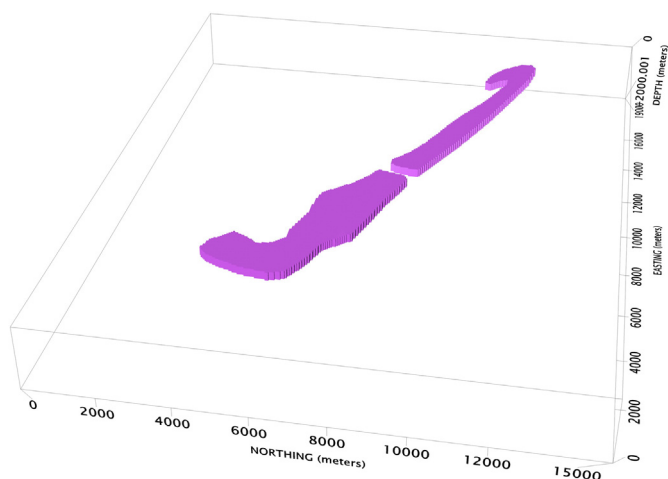
$x-$axis pointing north, $y-$axis pointing east, and $z-$axis pointing down. The density contrast within each prism is constant but unknown. Let $\mathbf{m}$ be an M-dimension vector of unknowns whose element $m_j$ is the density contrasts of the jth prism. The N-dimensional vector of predicted gravity-gradient data $\mathbf{d}$ produced by the density-contrast distribution $\mathbf{m}$ can be written in matrix notation as:

$$\mathbf{d} = \mathbf{Am} \qquad (1)$$

where $\mathbf{A}$ is an N x M sensitivity matrix whose $j^{th}$ column contains the gravity-gradient observations produced by the $j^{th}$ prism with unit density contrast.

### 2.1. The inverse problem

The inverse problem of estimating a discrete density-contrast distribution $\mathbf{m}$ from the gravity-gradient observations $\mathbf{d^o}$ is an ill-posed problem because its solution is neither unique nor stable. This means that there will be infinite solutions that fit the gravity-gradient data. To reduce this ambiguity, the gravity-gradient inversions must introduce constraints on the anomalous mass distribution. These constraints allow a straightforward and versatile way to impose, on the solution, certain geological attributes. Because the gravity-gradient inversions use different constraints, they differ from each other in the particular bias imposed by the geologic information introduced through the constraints. In this work, we used two quite different gravity-gradient inversions which differ from each other by the imposed constraints. The first one will be named here as the *depth-weighting smoothing inversion* (Li, 2001) and the second is named *planting anomalous density inversion* (Uieda and Barbosa, 2012). In this section, we review these two gravity-gradient inversions.



Fig. 1. Simulated iron-ore formation (pink prisms) with density contrast of 0.75 g/cm$^3$. This model was inspired by geologic interpretations of the iron-ore deposit over the Gandarela syncline in Quadrilátero Ferrífero (Brazil).

## 2.2. Depth-weighting smoothing inversion (Li, 2001)

By using a least-squares constrained optimization problem, Li (2001) estimated a 3D density-contrast distribution by minimizing the objective function:

$$\Gamma(\mathbf{m}) = \phi_d + \mu\phi_m, \tag{2a}$$

subject to

$$m_j^{min} \leq m_j \leq m_j^{max}, \quad j = 1,...M, \tag{2b}$$
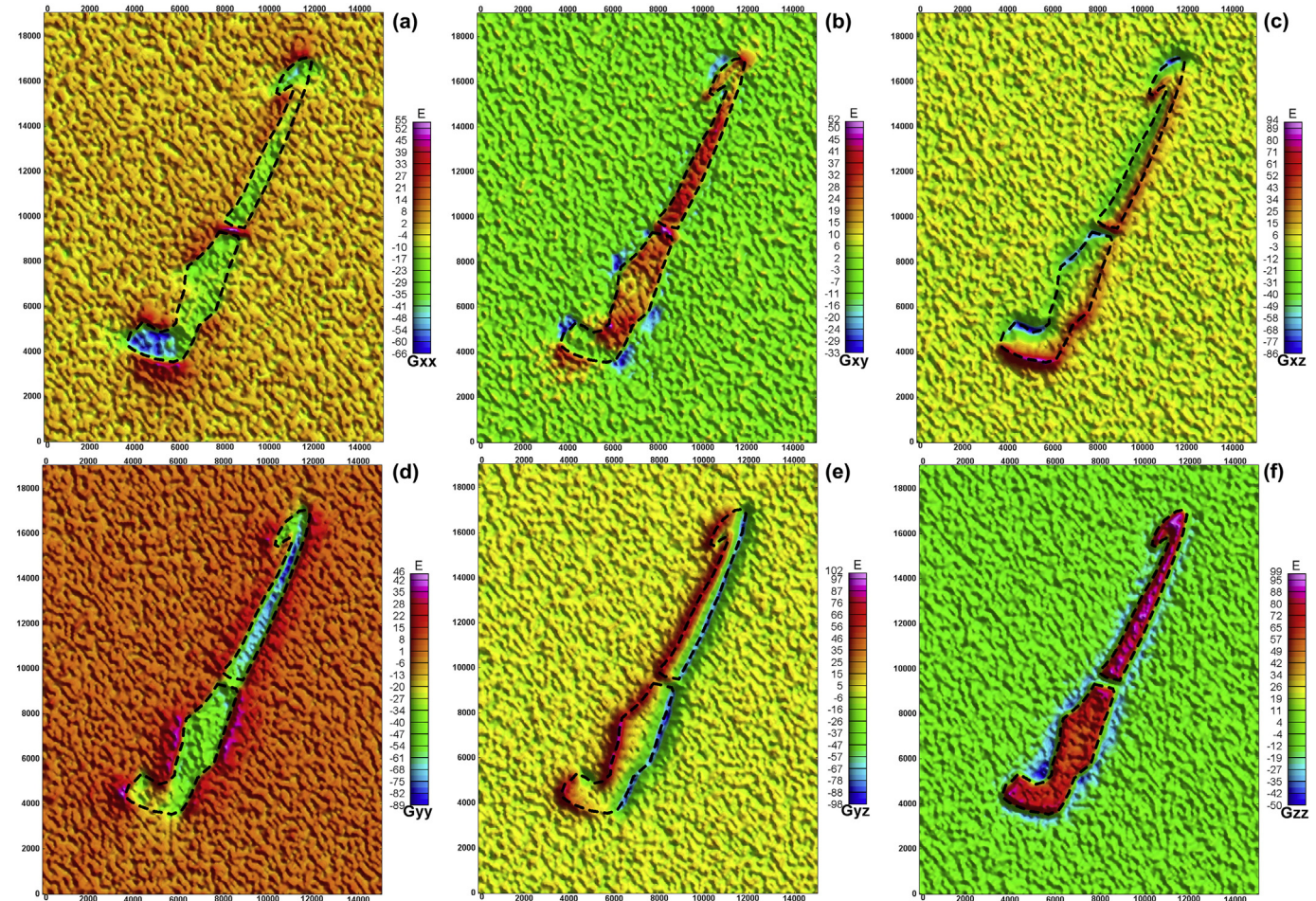
where $m_j^{min}$ and $m_j^{max}$ are, respectively, the lower and upper bounds for the density contrast estimate of the $j^{th}$ element $m_j$ of the parameter vector **m.** These bounds are defined element by element by the interpreter based on his a priori knowledge about the geology of the area.

In Eq. (2a), the function $\phi_d$ is the data-misfit weighting function, given by

$$\phi_d = \left\| W_d\left(d\text{-}d^0\right) \right\|_2^2, \tag{3}$$

where $\|.\|_2$ is the Euclidean norm and $\mathbf{W_d}$ is an N x N inverse data covariance matrix. The depth-weighting smoothing function $\phi_m$ was proposed by Li and Oldenburg (1996) in the continuous and discrete cases. The discrete formulation of this function can be written as

$$\boldsymbol{\phi_m} = \|\boldsymbol{W_m}(\boldsymbol{m}-\boldsymbol{m^o})\|^2 \tag{4}$$

where $\mathbf{m^o}$ is a prior reference parameter vector and $\mathbf{W_m}$ is an L x M weighting matrix given by

$$\mathbf{W_m} = \mathbf{W_\alpha DW_z} \tag{5}$$
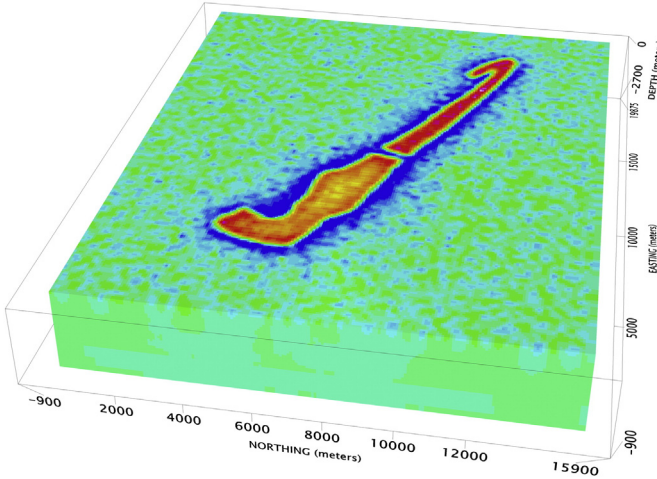
where **D** is an L x M matrix that can be partitioned as

$$D = \begin{bmatrix} I \\ D_x \\ D_y \\ D_z \end{bmatrix}, \tag{6}$$

where **I** is the identity matrix of order M and $\mathbf{D_x}$, $\mathbf{D_y}$, and $\mathbf{D_z}$ are matrices representing the first-order discrete differences along the $x-$, $y-$, and $z-$directions (Aster et al., 2013). In Eq. (5), $\mathbf{W_\alpha}$ is an L x L weighting matrix that can be partitioned as

$$W_a = \begin{bmatrix} a_s S_s \\ a_x S_x \\ a_y S_y \\ a_z S_z \end{bmatrix}, \tag{7}$$

where $\mathbf{S_i}$, $i = s, x, y$, and $z$, is a diagonal matrix whose elements $\sqrt{\varpi_i}$, $i = s, x, y$, and $z$, are weights assigned to the constraints. For $\mathbf{S_s}$ the values of $\omega_i$ are assigned to each prism. For $\mathbf{S_x}$, $\mathbf{S_y}$ and $\mathbf{S_z}$ the values of $\omega_i$ are assigned to each interface between adjacent prisms in the $x-$, $y-$, and $z-$directions, respectively. The role of the weights is to impose a certain degree of smoothness in the solution. The larger the value of



**Fig. 2.** Synthetic noise-corrupted (colored maps) (a) $g_{xx}-$, (b) $g_{xy}-$, (c) $g_{xz}-$ (d) $g_{yy}$, (e) $g_{yz}-$ and (f) $g_{zz}$ —components of the gravity-gradient tensor. The synthetic components are produced by the simulated body shown in Fig. 1 (pink prisms). The unit of measure for the gravity gradient is the Eötvös (E) where 1 E is equal to 0.1 mGal km$^{-1}$. The dashed black lines are the horizontal projections of the boundaries of the simulated iron-ore formation (Fig. 1).

**Fig. 3.** Perspective view of the estimated density-contrast distribution by inverting the $g_{zz}$ − component of the gravity gradient tensor (Fig. 2f) through the depth-weighting smoothing inversion.

the weights the smoother will be the estimates of density-contrast distribution. In Li (2001) and Li and Oldenburg (1996), the smoothing constraints are imposed over each interface between adjacent prisms of the interpretation model in the respective $x-$, $y-$, and $z-$directions. For example, the larger the value of the weights in the $x-$direction, the smoother will be the variation of the density-contrast estimates along the $x-$direction leading to a smoothing distribution in the $x-$direction (north direction). In Eq. (7), $\alpha_s, \alpha_x, \alpha_y$ and $\alpha_z$ are positive scalars that control the global importance of the constraints. In Eq. (5), the M x M diagonal matrix $\mathbf{W_Z}$ represents the discretized form of the continuous depth-weighting function given by

$$f(z) = \frac{1}{(z+z_o)^{\beta/2},} \tag{8}$$

where $z$ is the depth of each layer of prisms which compose the discretization mesh of the subsurface, $z_o$ depends upon the observation height and prism size and $\beta$ is a scalar chosen to approximate

the decaying with $z$ at the same rate as the gravity-gradient kernel of a 3D prism at a given depth $z$.
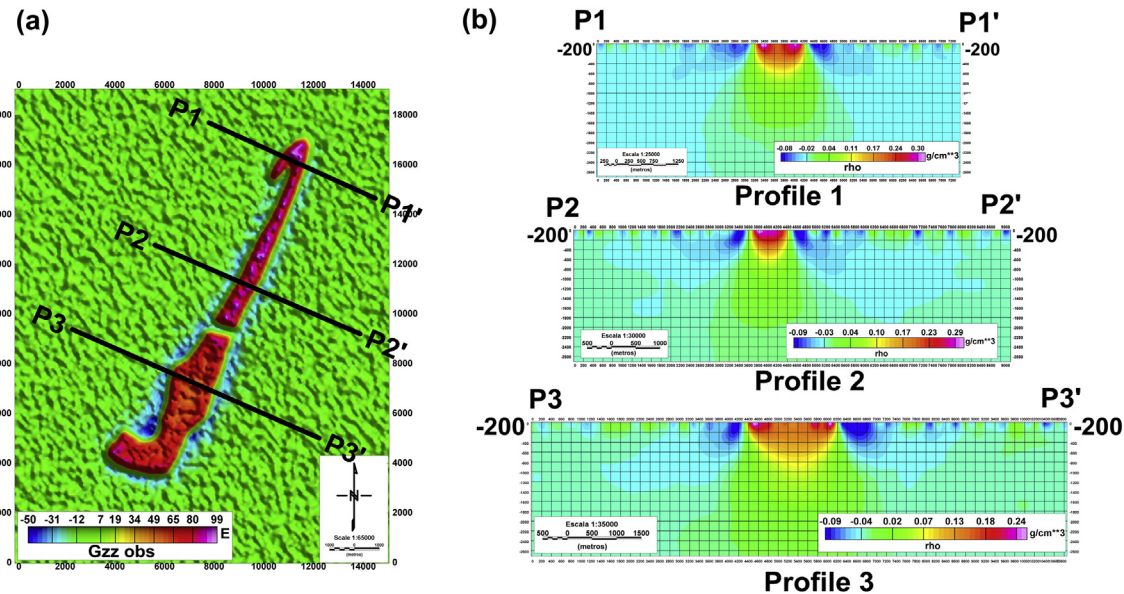
The depth-weighting smoothing inversion constrains the solution to be buried, through the penalization of outcropping sources, which is achieved by weighting the density-contrast estimates (Eq. (4)). In addition, this inversion constrains density-contrast estimates to lie between the upper and lower bounds imposed by the inequality (2b) constraints . The weights (Eq. (8)) penalize the large estimated densities located between the Earth's surface and the source's top. Indirectly, the source's top is controlled by the scalars β and $z_o$ (Eq. (8)) and thus, the efficacy of this method lies in the prior knowledge about the depth of the source's top. Notice that this method imposes a smoothing density-contrast distribution subject to fitting the observations within the measurement errors (function $\phi_d$, Eq.(3)). By assuming that the background has density contrast equal to zero, the inequality (2b) constraint should include this value; otherwise, the estimated density-contrast distribution yields an unacceptable data fit.

Although, the depth-weighting smoothing function $\phi_m$ (Eq. (4)) is a regularizing function, we call it, from now on, as constraint function.
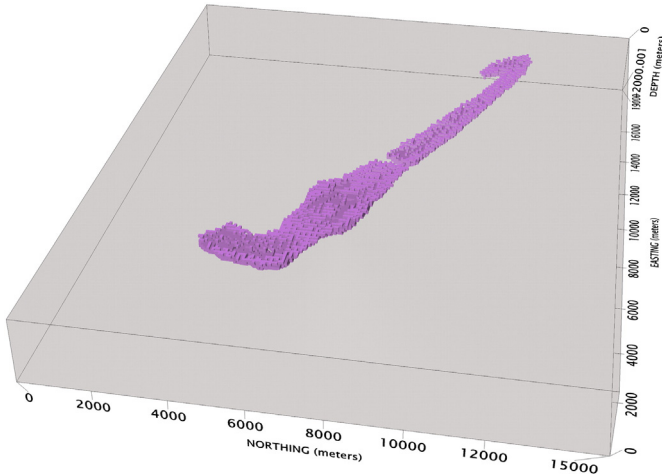
### 2.3. Planting anomalous density inversion (Uieda and Barbosa, 2012)

By using a systematic search algorithm, Uieda and Barbosa (2012) estimated a 3D density-contrast distribution by aggregating small prisms with given non-null density contrasts around user specified prisms called "seeds". The seeds operate as gross skeletal outlines of the geologic bodies. Iteratively, the solution grows by the successive accretion of new prisms located in the immediate vicinity of the current solution. At each iteration of the growth scheme, a candidate prism to be accreted will be one of the neighboring prisms of the current solution. Only one prism at a time can be accreted to the solution. The prism chosen to be accreted is one whose addition both reduces the data-misfit function and produces the smallest value of the goal function $\Gamma(m)$ (Eq. (2a)). The data-misfit function used by Uieda and Barbosa (2012) is

$$\phi_d = \left\| d - d^0 \right\|_1, \tag{9a}$$



**Fig. 4.** (a) The observed $g_{zz}$ − component of the gravity gradient tensor (Fig. 3f). The black lines P1–P1′, P2–P2′ and P3–P3′ establish the location of the vertical cross sections shown in Fig. 4b. (b) Vertical cross sections of the estimated density-contrast distribution (Fig. 3) produced by the depth-weighting smoothing inversion.

**Fig. 5.** Perspective view of the estimated density-contrast distribution by inverting the $g_{xx}-$ , $g_{xy}-$ , $g_{xz}-$ , $g_{yy}-$ , $g_{yz}-$ and $g_{zz}-$ components of the gravity gradient tensor (Fig. 2) through the planting anomalous density inversion.

with $\|.\|_1$ being the L1-norm. The regularizing function $\phi_m$ is given by

$$\phi_m = \frac{1}{f} \sum_{j=1}^{M} \frac{m_j}{m_j + \varepsilon} \ell_j, \tag{9b}$$

where $\varepsilon$ is a small positive constant, $f$ is a scaling factor equal to the mean extent of the region in the subsurface to be interpreted and $\ell_j$ is the distance between the $j^{\text{th}}$ prism and the seed which has undergone its accretion. The regularizing function (Eq. (9b)) was inspired by Silva Dias et al. (2009). The main advantage of planting anomalous density inversion is its computational efficiency, requiring little computer memory and processing time. This inversion method requires neither the full computation and storage of a sensitivity matrix **A** (Eq. (1)) nor the solution of large equation systems.

The planting anomalous density inversion constrains the solution to be compact. The regularizing function (Eq. (9b)) imposes the compactness on the solution and the concentration of the estimated anomalous densities around the seeds. Explicitly, the depths of the geologic bodies are controlled by the depth of the seeds and thus, the efficacy of this

method lies in the proper choice of the seeds (their depths and density contrasts). Usually, the choice of density contrast of a seed is not critical and it must be grounded on the prior knowledge about the rocks of the study area. Like the depth-weighting smoothing inversion (Li, 2001), the planting anomalous density inversion depends on the prior knowledge about the depth of the geologic bodies.

## 3. Application to synthetic data
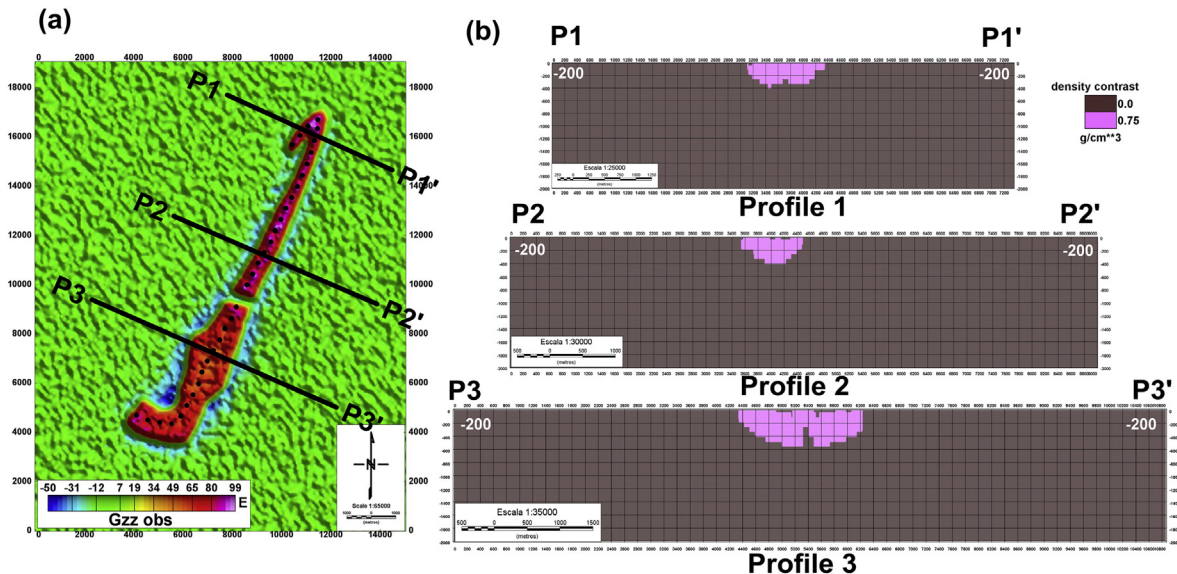
### 3.1. Simulating the known characteristics of the Gandarela syncline iron ore

We illustrate the performance of the above-mentioned gravity-gradient inversion methods by applying it to a simulated iron-ore body with the known characteristics of the ore deposit within the flank of the Gandarela syncline in Quadrilátero Ferrífero (Brazil). These characteristics are: (i) the geometry of the horizontal projection of its boundaries; (ii) the mean depth and; (iii) the density contrast of the iron-ore body with the main host rocks based on our geological knowledge about the Quadrilátero Ferrífero. The simulated discontinuous iron-ore formation (Fig. 1) is made up of two 3D right prisms with depth to the top at 50 m and thickness of 250 m. These prisms have polygonal horizontal cross-sections simulating a banded iron formation (BIF), the so-called itabirites, with density of 3.11 g/cm$^3$ which is hosted in low-density rocks with a density of 2.36 g/cm$^3$. This implies that the density contrast of the simulated iron-ore body (Fig. 1) with the main host rocks is 0.75 g/cm$^3$. We stress that the discontinuity of the iron-ore formation simulates a geologic fault zone.
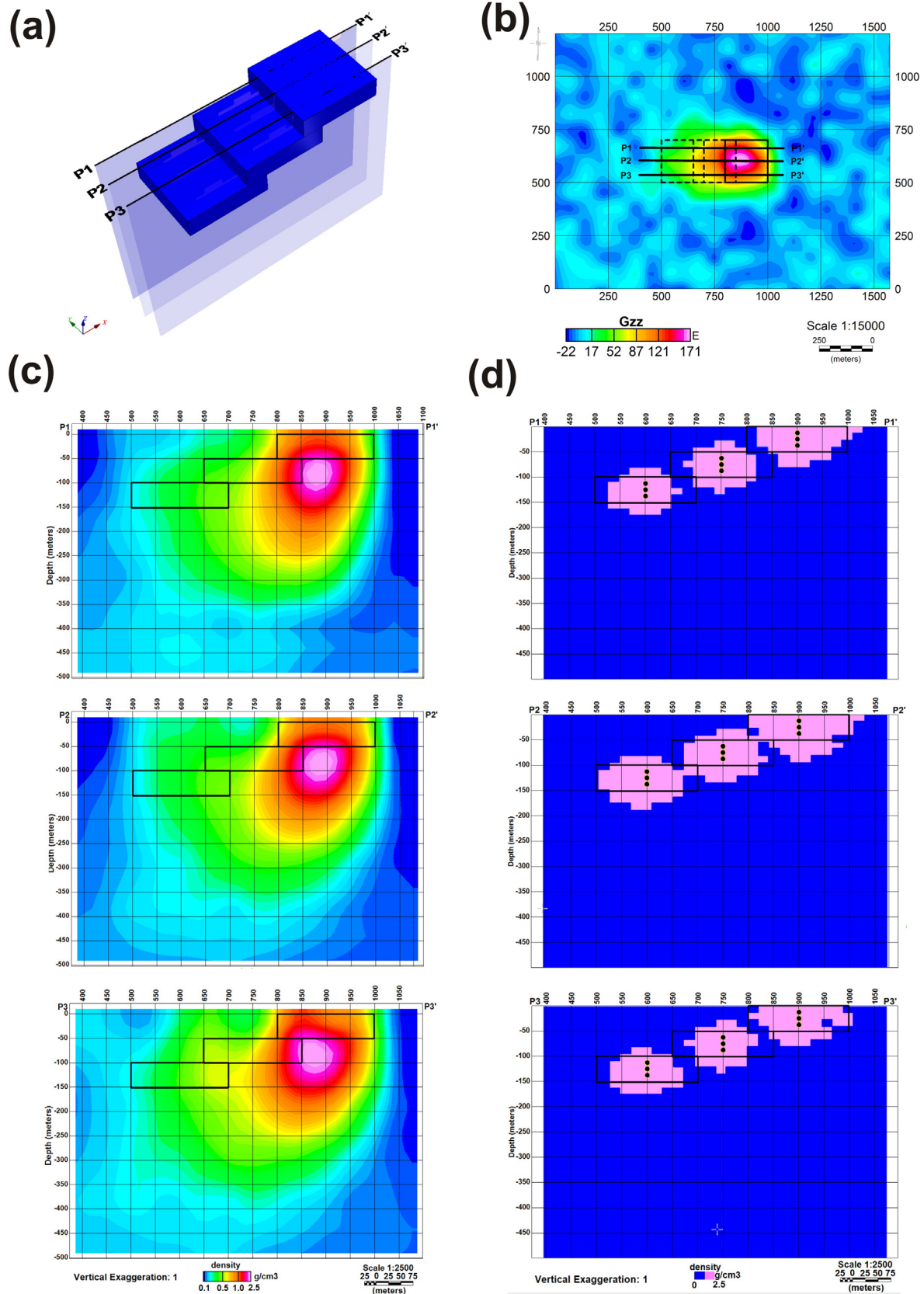
We computed the synthetic noise-corrupted data (color scale maps in Fig. 2) of the $g_{xx}-$ , $g_{xy}-$ , $g_{xz}-$ , $g_{yy}-$ , $g_{yz}-$ and $g_{zz}-$ components of the gravity-gradient tensor produced by the simulated iron-ore formation shown in Fig. 1. In this test, each component was calculated at 100 m height on a regular grid of $100 \times 100$ observation points in the $x-$ and $y-$ directions, totalling 10.000 observations, with a grid spacing of 0.15 km and 0.19 along the $x-$ and $y-$ directions, respectively. The data were contaminated with pseudorandom Gaussian noise with zero mean and standard deviation of 5 Eötvös.

### 3.1.1. Depth-weighting smoothing inversion (Li, 2001)
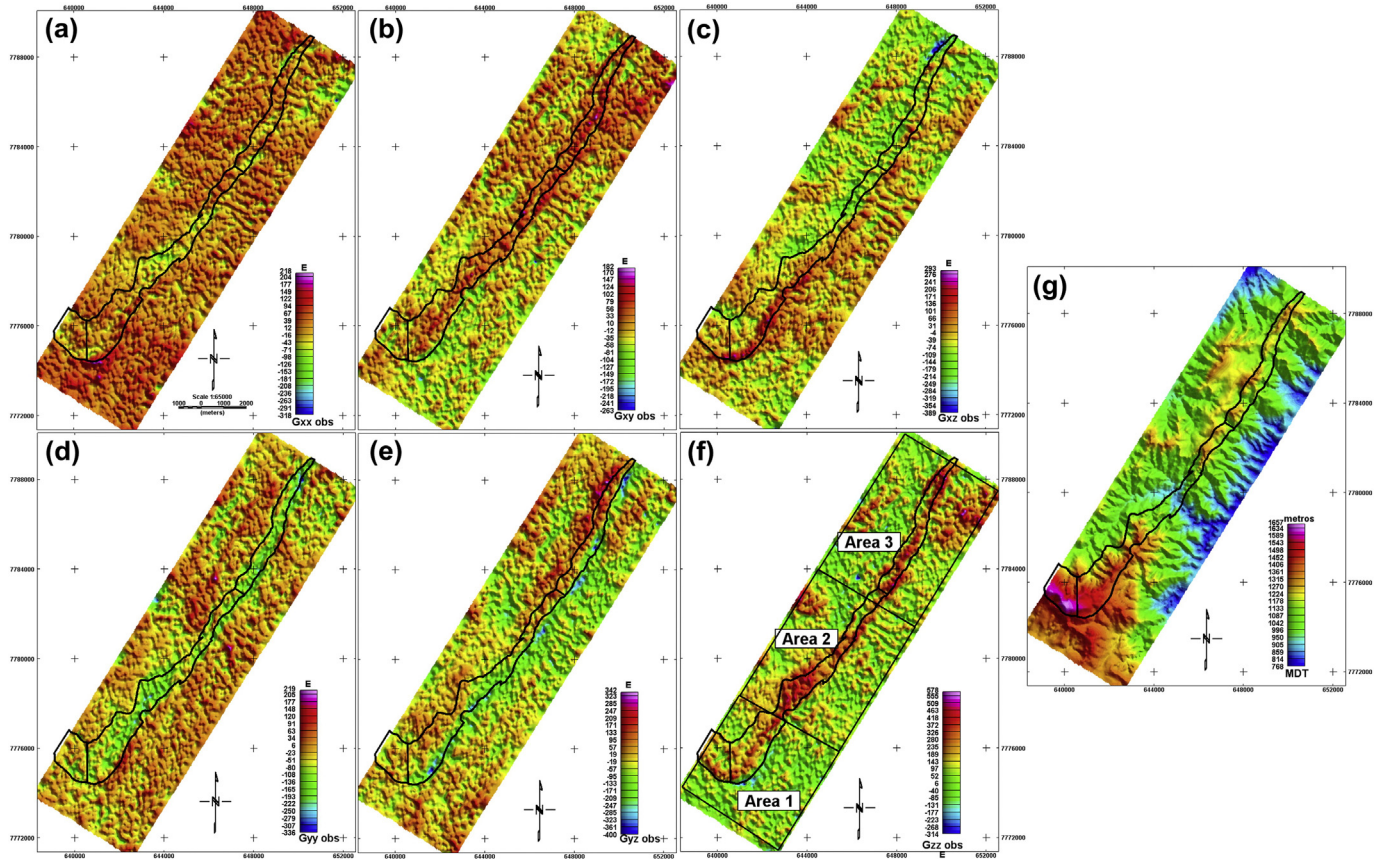
To apply the depth-weighting smoothing inversion, we select the subsurface volume containing the iron-ore formation with dimensions equal to 19 km, 15 km and 2 km along the $x-$ , $y-$ , and $z-$ directions,



**Fig. 6.** (a) The observed $g_{zz}-$ component of the gravity gradient tensor (Fig. 3f). The black dots show the horizontal coordinates of the seeds used in the inversion. The black lines P1–P1′, P2–P2′ and P3–P3′ establish the location of the vertical cross sections shown in Fig. 6b. (b) Vertical cross sections of the estimated density-contrast distribution (Fig. 5) produced by the planting anomalous density inversion using a set of seeds whose horizontal coordinates are shown in Fig. 6a as black dots.

**Fig. 7.** (a) Simulated dipping body with density contrast of 2.5 g/cm³. (b) Noise-corrupted $g_{zz}$ − component produced by dipping body shown in (a). Vertical cross sections of the estimated density-contrast distribution produced by (c) the depth-weighting smoothing inversion and (d) the planting anomalous density inversion using a set of seeds (black dots).

**Fig. 8.** Observed (a) $g_{xx}-$,(b) $g_{xy}-$ , (c) $g_{xz}-$, (d) $g_{yy}-$, (e) $g_{yz}-$ and (f) $g_{zz}-$components of the airborne gravity-gradient data over the southern flank of the Gandarela syncline in Quadrilátero Ferrífero (Brazil). The thick black lines delineate the mapped boundaries of the iron formation according to Dorr (1969). (g) The Digital Terrain Model (DTM) of the study area. The study area was divided into three areas (Areas 1–3) whose locations are shown in Fig. 8f.

respectively. To minimize the edge effects, we extend the horizontal limits of the subsurface volume beyond the limits of the synthetic data (Fig. 2) so that the grid of observations stay centralized. We discretized the subsurface volume along the $x-$, $y-$, and $z-$ directions into a mesh of cubes with side lengths of 75 m. Thus, the total number of prisms in the subsurface is about 1.3 million. This inversion algorithm requires the tuning of inversion control constants such as the regularizing
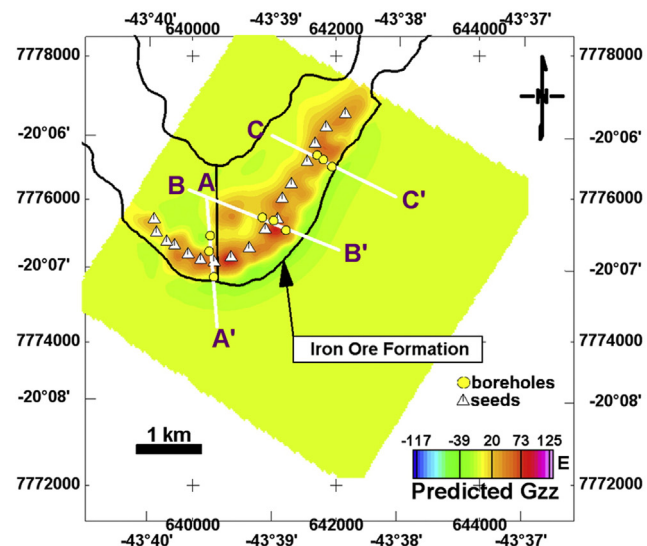
parameter ($\mu$ in Eq. (2a)), the initial approximation $\mathbf{m^o}$ to the density contrast vector, the upper and lower bounds to the density contrast, both assigned to each elementary prism according to inequality (2b). Because this inversion algorithm requires the full computation and storage of a large sensitivity matrix and the solution of a large equation system, we invert 10.000 observations of only $g_{zz}-$component of the gravity gradient tensor.
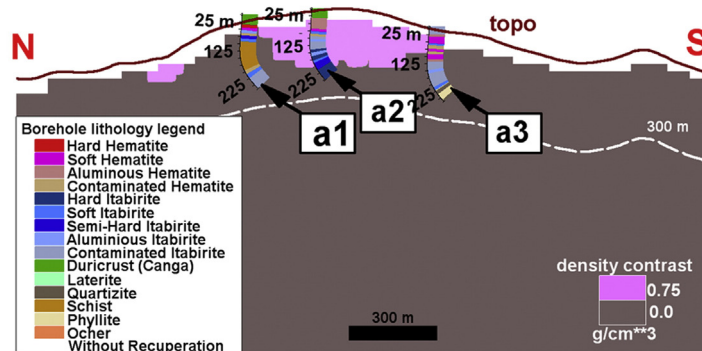
**Table 1**
Detailed variables of the Areas 1–3 whose locations are shown in Fig. 8f. These variables were used in the two inversions: 1) planting anomalous density inversion and 2) depth-weighting smoothing inversion.

| | Detailed variables of the Areas 1–3 | Planting anomalous density inversion Uieda and Barbosa (2012) | Depth-weighting smoothing inversion Li (2001) |
|---|---|---|---|
| | Number of components to be inverted | 6 | 3 |
| A | Number of observations for each | 3975 | 3975 |
| R | component | | |
| E | Number of observations to be inverted | 23,850 | 11,925 |
| A | Mesh of 3D prisms | $225 \times 227 \times 52$ | $140 \times 139 \times 37$ |
| 1 | Total number of prisms | 2,655,900 | 720,000 |
| | Number of components to be inverted | 6 | 3 |
| A | Number of observations for each | 5288 | 5288 |
| R | component | | |
| E | Number of observations to be inverted | 31,728 | 15,864 |
| A | Mesh of 3D prisms | $264 \times 257 \times 43$ | $157 \times 163 \times 37$ |
| 2 | Total number of prisms | 2,917,464 | 950,000 |
| | Number of components to be inverted | 6 | 3 |
| A | Number of observations for each | 5.710 | 5.710 |
| R | component | | |
| E | Number of observations to be inverted | 34.260 | 17.130 |
| A | Mesh of 3D prisms | $258 \times 281 \times 41$ | $160 \times 172 \times 37$ |
| 3 | Total number of prisms | 2,972,418 | 1,018,240 |

**(a)**

**(b)**

Borehole lithology legend
- Hard Hematite
- Soft Hematite
- Aluminous Hematite
- Contaminated Hematite
- Hard Itabirite
- Soft Itabirite
- Semi-Hard Itabirite
- Aluminious Itabirite
- Contaminated Itabirite
- Duricrust (Canga)
- Laterite
- Quartizite
- Schist
- Phyllite
- Ocher
- Without Recuperation

density contrast
0.75
0.0
g/cm**3

**A - A' Profile**

**(c)**

Borehole lithology legend
- Soft Hematite
- Aluminous Hematite
- Contaminated Hematite
- Hard Itabirite
- Soft Itabirite
- Semi-Hard Itabirite
- Aluminious Itabirite
- Contaminated Itabirite
- Duricrust (Canga)
- Laterite
- Intrusive
- Phyllite
- Ocher
- Without Recuperation

density contrast
0.75
0.0
g/cm**3

**B - B' Profile**

**(d)**

Borehole lithology legend
- Soft Hematite
- Goethitic Hematite
- Aluminous Hematite
- Hard Itabirite
- Soft Itabirite
- Semi-Hard Itabirite
- Goethitic Itabirite
- Contaminated Itabirite
- Duricrust (Canga)
- Laterite
- Phyllite
- Ocher

density contrast
0.75
0.0
g/cm**3

**C - C' Profile**

Firstly, we used the Tikhonov curve or L-curve (Hansen, 1992) to choose as the best regularizing parameter (μ in Eq. (2a)) the one that better controls the trade-off between the data-misfit function (ϕ_d in Eq. (2a)) and the regularizing function (ϕ_m in Eq. (2a)). However, this curve has fails. Then, we adopted the maximum curvature of the L-curve (Hansen, 1992) to choose the best regularizing parameter. The curvature of the L-curve as a function of the regularizing parameter shows the point of maximum at μ = 1. To all elements of the prior reference parameter vector **m°** (Eq. (4)), we set the value 0.5 g/cm$^3$. To all M prisms that set up the discretization mesh of the subsurface, the lower and upper bounds (Eq. (2b)) for the density contrast estimate are -0.1 g/cm$^3$ and 0.75 g/cm$^3$, respectively. This wide range of the density contrasts was chosen to approximately honor the interval of the density contrasts of the targeted (0.75 g/cm$^3$) and non-targeted (0.0 g/cm$^3$) rocks simulated in this test. In addition, this range of the density contrasts the estimated density-contrast distribution yields an acceptable data fit.

Fig. 3 displays a perspective view of the 3D estimated density-contrast distribution by inverting the $g_{zz}$ −component of the gravity gradient tensor through the depth-weighting smoothing inversion. This estimated density-contrast distribution exhibits a smooth variation that smears out the boundaries of the iron-ore bodies. Hence, this solution retrieves the boundaries of the simulated iron-ore formation. Fig. 4 shows three vertical cross sections (P1–P1′–P3–P3′) of the 3D estimated density-contrast distribution using the depth-weighting smoothing inversion. The black lines in Fig. 4a display the locations of these vertical cross sections. Notice that the largest density-contrast estimates are restricted to 300 m deep being consistent with the true depth of the simulated iron-ore formation. However, the largest density-contrast estimates are smaller than the true value (0.75 g/cm$^3$).

### 3.1.2. Planting anomalous density inversion (Uieda and Barbosa, 2012).

To apply the planting anomalous density inversion, we select the same subsurface volume used in the previous inversion (i.e., 19 km, 15 km and 2 km along the $x−$, $y−$, and $z−$ directions, respectively). We used 34 seeds with density contrast equal to 0.75 g/cm$^3$ and placed at the depth of 175 m. The horizontal locations of the seeds were chosen based on the positive anomalies of the $g_{zz}$ −component of the gravity-gradient data. In contrast with the depth-weighting smoothing inversion, in which only the $g_{zz}$ −component of the gravity gradient tensor was inverted, in the planting anomalous density inversion all the six components of the gravity gradient tensor were inverted. Hence, we invert 60.000 observations of the $g_{xx}−$, $g_{xy}−$, $g_{xz}−$, $g_{yy}−$, $g_{yz}−$ and $g_{zz}$ −components of the gravity gradient tensor. This is possible because the planting anomalous density inversion requires neither the full computation and storage of a large sensitivity matrix nor the solution of a large equation system. Fig. 5 shows a perspective view of the 3D estimated density-contrast distribution by inverting the six components of the gravity gradient tensor (Fig. 2) through the planting anomalous density inversion. This estimated density-contrast distribution displays steeper gradients close to the true borders of the simulated iron-ore formation (Fig. 2) retrieving its horizontal projection perfectly. Fig. 6 shows three vertical cross sections (P1–P1′–P3–P3′) of the 3D estimated density-contrast distribution using the planting anomalous density inversion. The black lines in Fig. 6a display the location of these vertical cross sections and the black dots show the horizontal coordinates of the seeds used in the inversion. This inversion retrieves homogeneous and compact iron-ore bodies with a single density contrast equal to 0.75 g/cm$^3$. This solution yields a reasonable estimation of the geometry of the simulated iron-ore formation.

### 3.2. Simulating a dipping body

We computed the noise-corrupted components of the gravity-gradient tensor (not shown) produced by a synthetic body simulating a dipping body shown in Fig. 7a. Here, we inverted the $g_{zz}$ −component of the gravity-gradient data using the depth-weighting smoothing inversion (Li, 2001) and the planting anomalous density inversion (Uieda and Barbosa, 2012). This synthetic test aims to analyze the ability of these methods to detect dipping bodies. Fig. 7c shows a slice through the 3D estimated density-contrast distribution from Li's (2001) inversion. The solution from the smoothing inversion correctly retrieves the dip direction of the dike, but it does not retrieve its dip angle. Fig. 7d shows a slice through the 3D estimated density-contrast distribution from the planting anomalous density inversion (Uieda and Barbosa, 2012). Notice that solution from the planting anomalous density inversion yields a homogeneous and compact model of the iron-ore allowing the assessment of the volume of the iron ore.

## 4. Application to gravity gradient anomalies of Gandarela syncline

The study area is located within part of the southern flank of the Gandarela syncline which is a megastructure of the Quadrilátero Ferrífero in southeastern Brazil with the highest perspectives for iron ore exploration. The Gandarela syncline has a northeast–southwest trend being fractionized by Brazilian faults. Most of the iron-ore bodies in the Quadrilátero Ferrífero are hosted in the oxided, metamorphosed and heterogeneously deformed banded iron formation (BIF) of the Cauê Formation, the so-called itabirites. The BIF of the Cauê Formation comprises a 250–300 m thick sequence of altered sedimentary deposits that are made up of alternating layers of silica and hematite–magnetite, as well as carbonates and iron silicates.
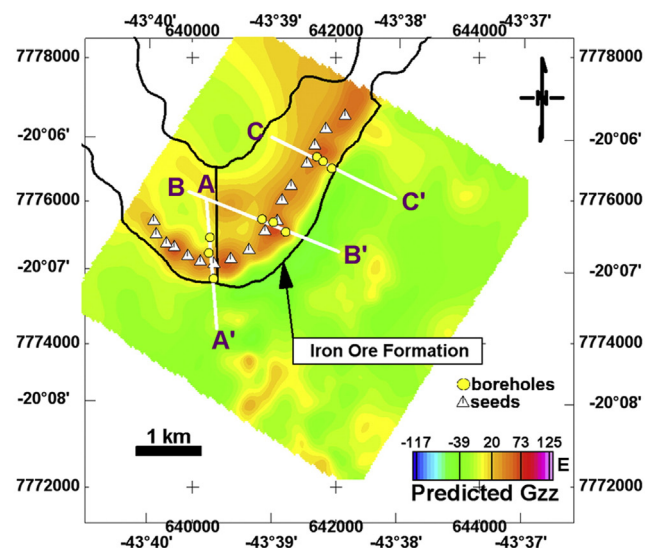
The airborne gravity gradiometry data were acquired in 2005 over the study area covering 95 km$^2$ with dimensions of approximately 19 km by 5 km. This airborne survey was flown with a semi-draped flight pattern at heights ranging from 57 to 582 m above the topographic surface, having 50 flight lines along northeast–southwest direction with line spacing of 100 m. The gravity-gradient data were preprocessed that includes the correction of the gravity-gradient signals produced by the terrain using a density of 2.36 g.cm$^{-3}$. Each component of the gravity-gradient data contains 15,275 observations, totaling 91,650. Fig. 8 shows the preprocessed gravity-gradient data.

The depth-weighting smoothing inversion (Li, 2001) and the planting anomalous density inversion (Uieda and Barbosa, 2012) were applied to interpret the iron-ore deposit at the southern flank of the Gandarela syncline in Quadrilátero Ferrífero (Brazil). The six components of the gravity gradient tensor were jointly inverted by using the planting anomalous density inversion whereas three components of the gravity gradient tensor ($g_{yy}−$, $g_{yz}−$ and $g_{zz}$ −components) were jointly inverted by using the depth-weighting smoothing inversion. The study area was divided into three areas named Areas 1–3 whose locations are shown in Fig. 8f. Table 1 shows the specifications of each area with respect to the number of gravity-gradient observations and the discretization mesh of 3D prisms.
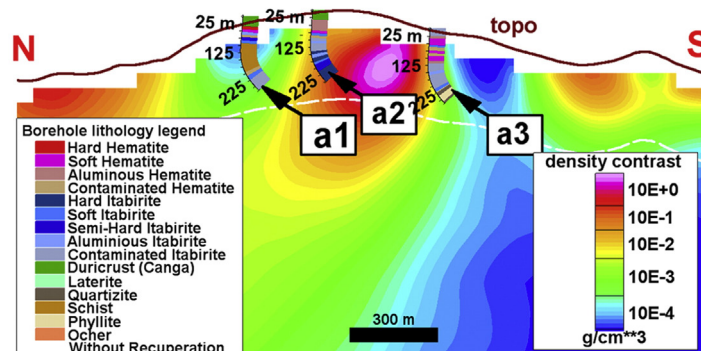
For all three areas, the itabirite and hematite are considered the targeted iron-ore rocks with an average density of 3.11 g/cm$^3$ and the non-targeted rocks (e.g., duricrust, laterite, quartizite, schist, phyllite, and ocher) have an average density of 2.36 g/cm$^3$; thus, the density contrast of the iron-ore body with the main host rocks is 0.75 g/cm$^3$. In the planting anomalous density inversion all seeds were assigned a target density contrast of 0.75 g/cm$^3$. The seeds were placed at the

Fig. 9. Area 1 − Inversion results using the planting anomalous density inversion. After Carlos et al. (2014). The predicted $g_{zz}$ −component of the gravity gradient tensor by using the inversion is shown by the color map (upper panel). The thick black lines (upper panel) delineate the mapped boundaries of the iron formation according to Dorr (1969). The white lines AA′, BB′, and CC′ (upper panel) indicate the locations of the vertical cross sections shown in Figs. 9(b)-(d). The yellow dots and the white triangles (upper panel) show the horizontal coordinates of, respectively, the boreholes and the seeds used in the inversion. Vertical cross sections along profiles (b) AA′, (c) BB′, and (d) CC′ of the estimated density-contrast distribution with a single value of 0.75 g/cm$^3$ (in pink) and the lithological intervals (color ribbons) intersected by boreholes (a1–a3, b1–b3, c1–c3).
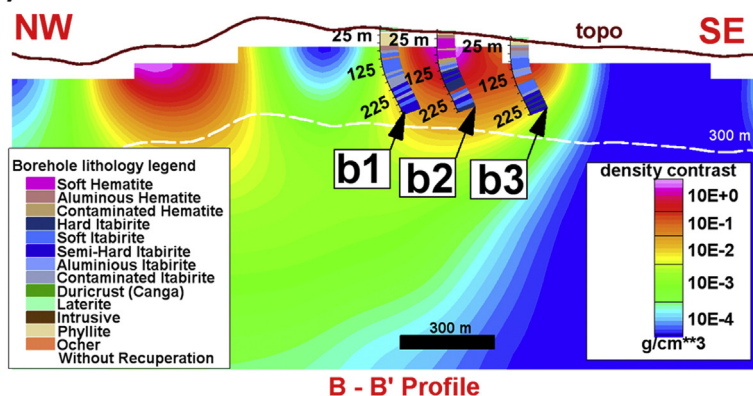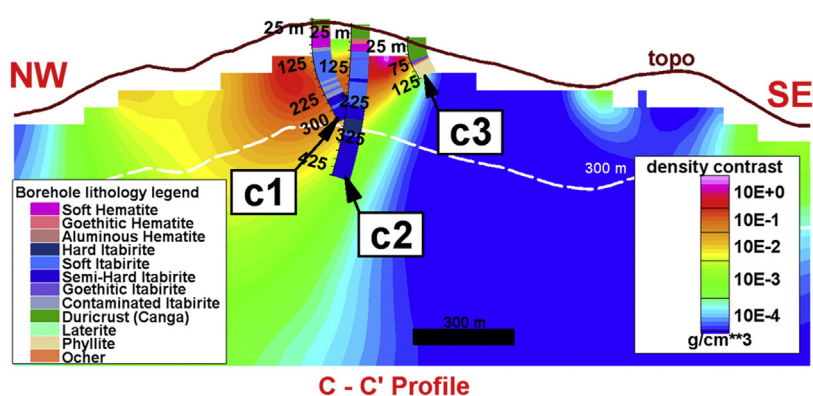
depths of 50 m, based on the overall information from the boreholes that the iron-ore deposit is shallow, and their horizontal locations were chosen based on the maxima of the $g_{zz}$ − component of the gravity-gradient data (Fig. 8f). In the depth-weighting smoothing inversion, all elements of the prior reference parameter vector $\mathbf{m^o}$ (Eq. (4)) were assigned the value 2.0 g/cm$^3$, the lower and upper bounds (Eq. (2b)) for the density contrast estimate were assigned -0.1 g/cm$^3$ and 3.31 g/cm$^3$, respectively. These values were chosen to approximately honor the interval of the density contrasts of the targeted and non-targeted rocks found in Quadrilátero Ferrífero.

Cross-sections of the density-contrast estimates over the Areas 1–3 are show in Figs. 9, 11 and 13 by using the planting anomalous density inversion and in Figs. 10, 12 and 14 by using the depth-weighting smoothing inversion. In these cross-sections, the lithologic intervals from drill holes (color-scaled ribbons) are superposed on the density-contrast estimates. In the color-scaled ribbons, the targeted iron-ore rocks are shown in red, magenta and the shades of blue. We expect that the large density-contrast estimates represent the estimated iron-ore mineralization. In the planting anomalous density inversion, the large estimate is 0.75 g/cm$^3$ (pink areas in Figs.9, 11, and13) and in the depth-weighting smoothing inversion the large estimate is variable as shown in Figs.10, 12, and 14. Hence, we expect the coincidence between the large density-contrast estimates and the targeted iron-ore rocks, which are the lithologies shown in red, magenta and the shades of blue in the color-scaled ribbons in Figs. 9–14.

### 4.1. Inversion results from Area 1

Figs. 9 and 10 show the cross-sections (AA′, BB′ and CC′) of the density contrast estimates over Area 1 produced by the planting anomalous densities and depth-weighting smoothing inversions, respectively. The upper panels of Figs 9 and 10 show the predicted $g_{zz}$ − component of the gravity gradient tensor produced, respectively, by the planting anomalous densities and depth-weighting smoothing inversions and the locations of the vertical cross sections AA′, BB′ and CC′.

The Area 1 is over a duricrust which is considered a non-targeted rock that is composed of high concentrations of iron oxides and iron hydroxides with high contents of iron, phosphorus and aluminum. However, the estimates obtained by both inversions (Figs. 9 and 10) and the boreholes found the iron ore in the subsurface. Most of the estimates agree reasonably well with the borehole information about the targeted rocks (iron-ore rocks shown in red, magenta and the shades of blue in the color-scaled ribbons, Figs. 9 and 10) which were drilled in the Area 1. The only exception is the borehole c2, which was drilled deeper to 450 m, going through a thick sequence of targeted rocks (the shades of blue in the color-scaled ribbons in Figs. 9d and 10d). However, the estimates obtained by both inversions (Figs. 9d and 10d) are a thinner mass of iron ore only 225 m thick.

The planting anomalous density inversion clearly reveals that the thickness and the width of the retrieved iron-ore body are variable (pink areas in Fig. 9b–d). This inversion method suggests that the iron-ore masses are dipping to the northwest direction. The northwest-dipping iron-ore body might, at most, be guessed from the cross-section BB′ (Fig. 9c).

Conversely, Fig. 10b–d shows that neither the thickness nor the width of the iron-ore body can be easily inferred by the depth-weighting smoothing inversion. This inversion produces a blurred density-contrast distribution that does not allow delineating the boundaries of the iron-ore body. Nevertheless, the existence of iron-ore masses dipping to northwest is easily evidenced from the

orientation of the smoother isovalue contours of the density-contrast estimates (Fig. 10b and c).

### 4.2. Inversion results from Area 2

Figs. 11 and 12 show the cross-sections (DD′, EE′ and FF′) of the density contrast estimates over Area 2 produced by the planting anomalous densities and depth-weighting smoothing inversions. The upper panels of Figs 11 and 12 show the predicted $g_{zz}$ − component of the gravity gradient tensor produced, respectively, by the planting anomalous densities and depth-weighting smoothing inversions and the locations of the vertical cross sections DD′, EE′ and FF′.

The estimates obtained by both inversions (Figs. 11 and 12) revealed different features of the iron-ore body. In contrast with the Area 1, the depth-weighting smoothing inversion clearly reveals that the estimated iron-ore body is not dipping in the southernmost limit of the Area 2 (Fig. 12b). Rather, this information is subtly suggested by the planting anomalous density inversion (Fig. 11b).

The estimates obtained by both inversions along the cross-sections DD′ and EE′ disagree. Along the vertical cross-section DD′, the planting anomalous density inversion estimates a thin iron-ore mass which agrees reasonably well with the information from borehole d1 (Fig. 11b). Rather, the depth-weighting smoothing inversion suggest the existence of a thick iron-ore mass (Fig. 12b); however, this estimate does not agree with the information from borehole d1. Along the vertical cross-section EE′, the estimated iron-ore mass via the planting anomalous density inversion (Fig. 11c) is thick attaining a maximum bottom depth of 300 m and extends to the northwest with a horizontal width of about 1 km; while the estimated iron-ore mass via the depth-weighting smoothing inversion (Fig. 12c) is shallow and with a horizontal width of about 300 m. Neither estimates (Figs. 11c and 12c) predicted thick iron-ore masses close to borehole e2 in disagreement with the drilled 325 m thick sequence of iron formations.

Along the vertical cross-section FF′, the estimated iron-ore mass by the planting anomalous density inversion (Fig. 11d) agrees reasonably well with the estimate obtained by the depth-weighting smoothing inversion (Fig. 12d). Both estimated iron-ore masses are shallow and extend to the southeast. The depth-weighting smoothing inversion clearly reveals that the estimated iron-ore body is dipping to the southeast (Fig. 12d) in the northernmost limit of the Area 2 (FF′ in Fig. 12a).
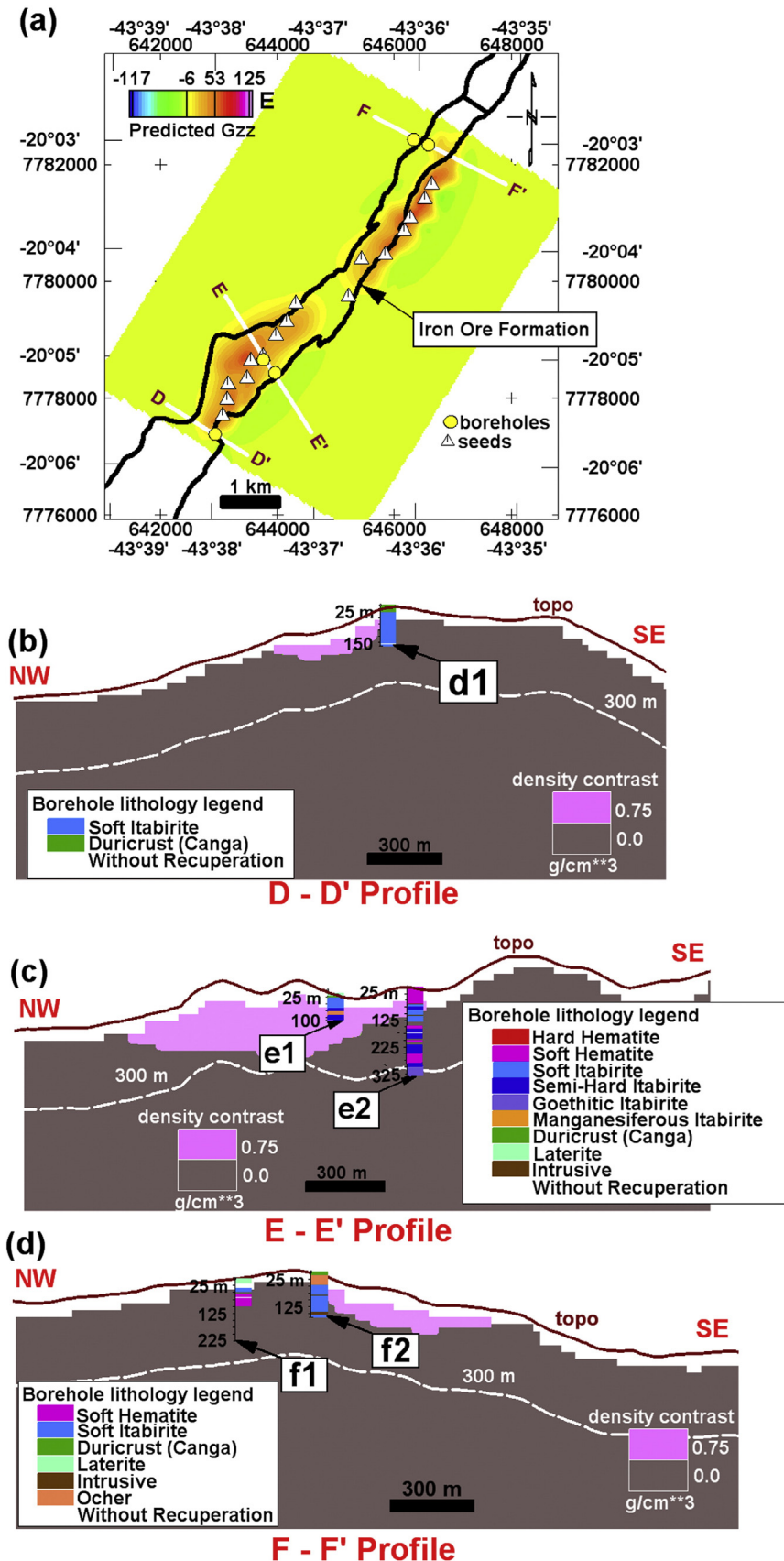
### 4.3. Inversion results from Area 3

Figs. 13 and 14 show the cross-sections (GG′, HH′ and II′) of the density contrast estimates over Area 3 produced by the planting anomalous densities and depth-weighting smoothing inversions. The upper panels of Figs 13 and 14 show the predicted $g_{zz}$ − component of the gravity gradient tensor produced, respectively, by the planting anomalous densities and depth-weighting smoothing inversions and the locations of the vertical cross sections GG′, HH′ and II′.
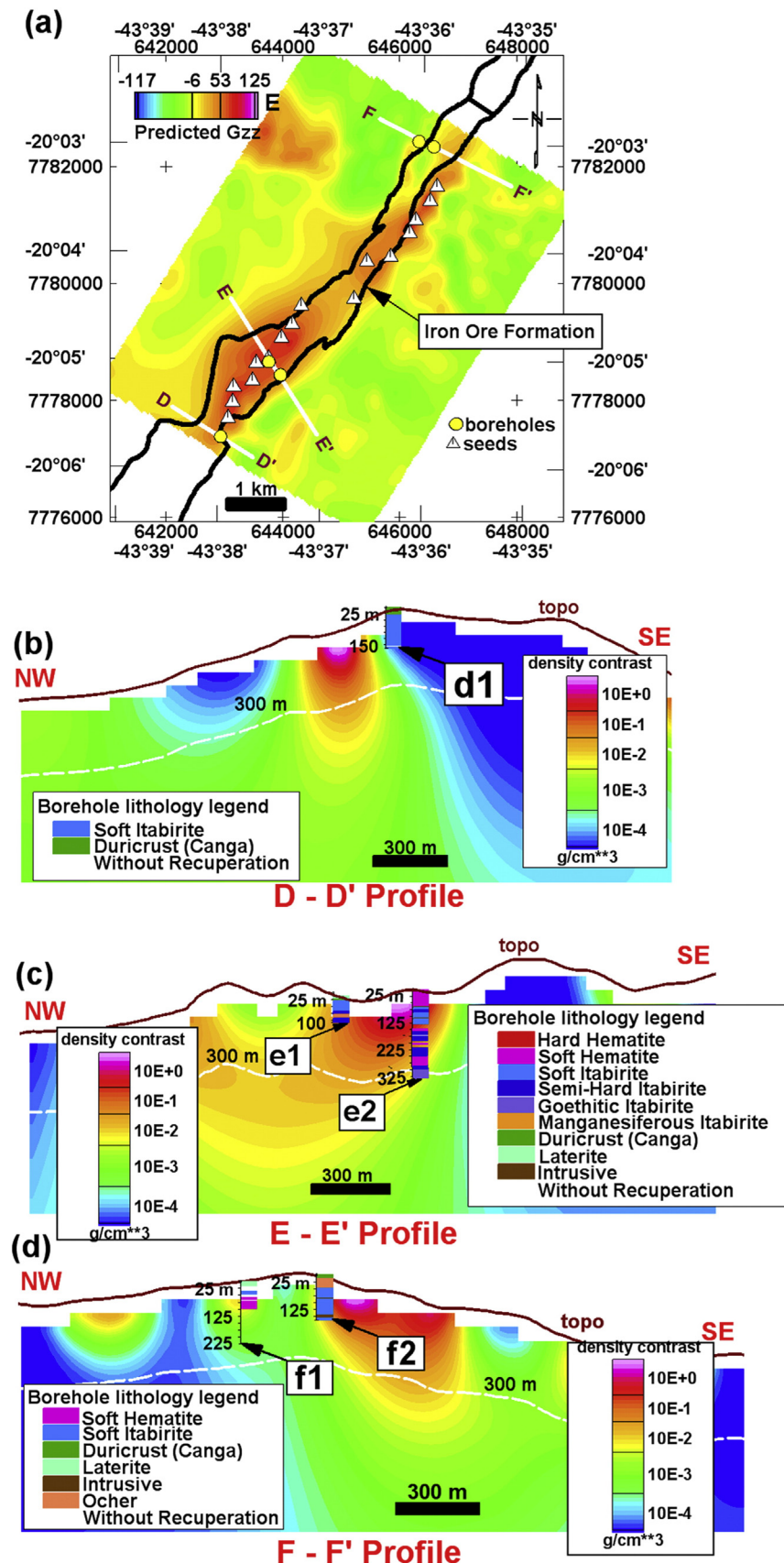
Along the vertical cross-sections GG′, HH′ and II′, the estimated iron-ore mass by the planting anomalous density inversion (Fig. 13b–d) agrees reasonably well with the estimate obtained by the depth-weighting smoothing inversion (Fig. 14b–d). Most of the Area 3 is covered by outcropping duricrust which is a non-targeted source in the study area. However, the estimated iron-ore masses by both inversions (Figs. 13b–d and 14b–d) predict iron ore in the subsurface.

In the southernmost limit of Area 3, the estimated iron-ore masses obtained by both inversions extend to the southeast. This southeastern extension along cross-section GG′ (Figs. 13b and 14b) agrees with the
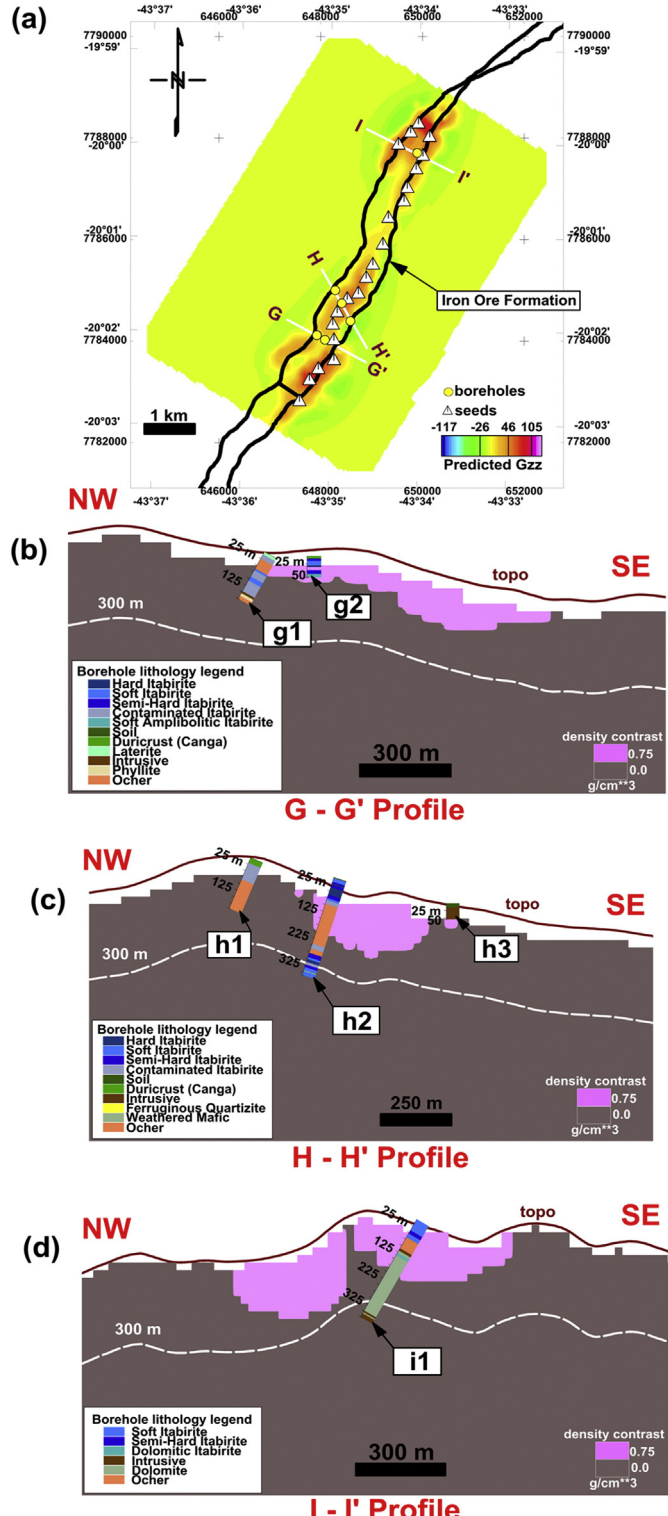
**Fig. 10.** Area 1 — Inversion results using the depth-weighting smoothing inversion. The predicted $g_{zz}$ − component of the gravity gradient tensor by using the inversion is shown by the color map (upper panel). The thick black lines (upper panel) delineate the mapped boundaries of the iron formation according to Dorr (1969). The white lines AA′, BB′, and CC′ (upper panel) indicate the locations of the vertical cross sections shown in Figs. 10(b)–(d). The yellow dots (upper panel) show the horizontal coordinates of the boreholes. Vertical cross sections along profiles (b) AA′, (c) BB′, and (d) CC′ of the estimated density-contrast distribution (in color) and the lithological intervals (color ribbons) intersected by boreholes (a1–a3, b1–b3, c1–c3).
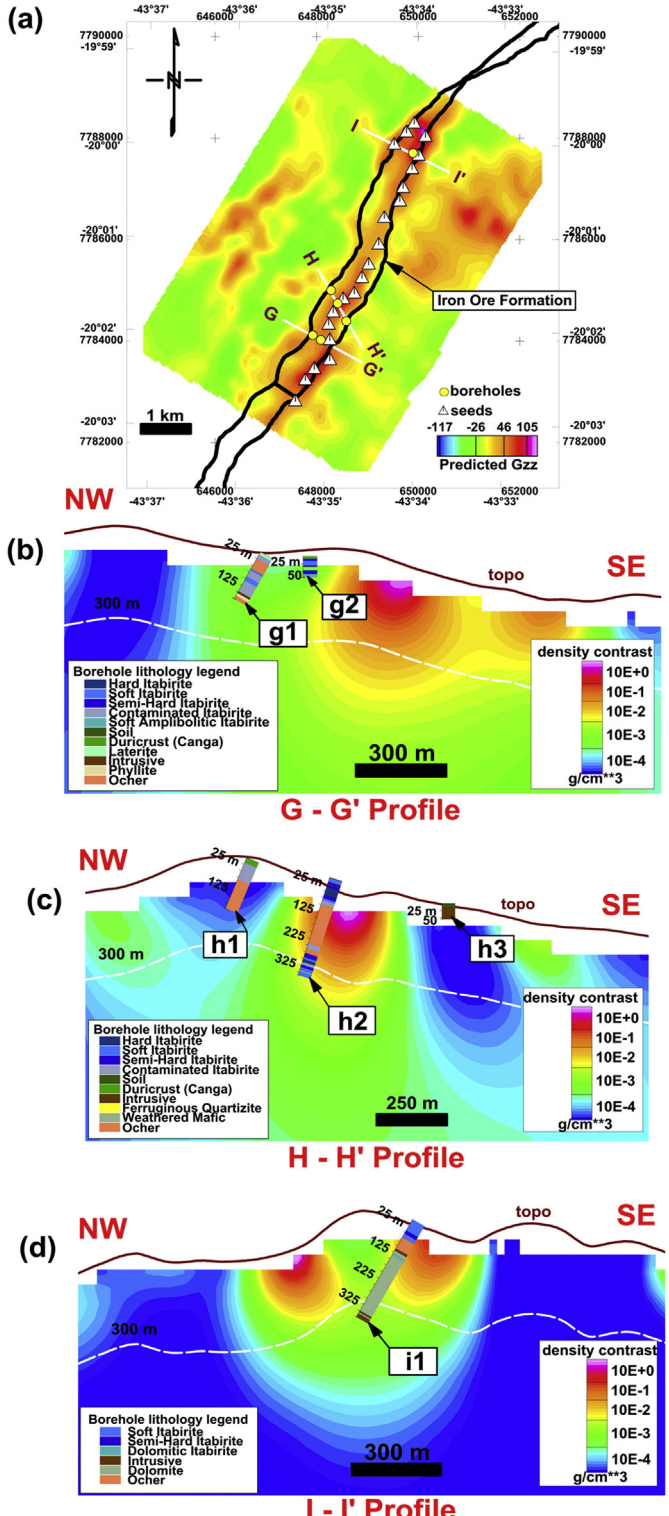
**Fig. 11.** Area 2 — Inversion results using the planting anomalous density inversion. After Carlos et al. (2014). The predicted $g_{zz}$ −component of the gravity gradient tensor by using the inversion is shown by the color map (upper panel). The thick black lines (upper panel) delineate the mapped boundaries of the iron formation according to Dorr (1969). The white lines DD′, EE′, and FF′ (upper panel) indicate the locations of the vertical cross sections shown in Figs. 11(b)-(d). The yellow dots and the white triangles (upper panel) show the horizontal coordinates of, respectively, the boreholes and the seeds used in the inversion. Vertical cross sections along profiles (b) DD′, (c) EE′, and (d) FF′ of the estimated density-contrast distribution with a single value of 0.75 g/cm³ (in pink) and the lithological intervals (color ribbons) intersected by boreholes (d1, e1, e2, f1, and f2).
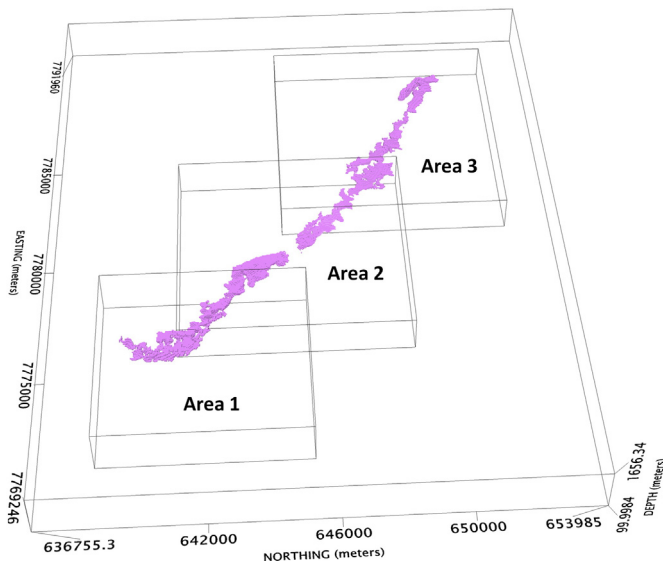
**Fig. 12.** Area 2 — Inversion results using the depth-weighting smoothing inversion. The predicted $g_{zz}$ — component of the gravity gradient tensor by using the inversion is shown by the color map (upper panel). The thick black lines (upper panel) delineate the mapped boundaries of the iron formation according to Dorr (1969). The white lines DD′, EE′, and FF′ (upper panel) indicate the locations of the vertical cross sections shown in Figs. 12(b)-(d). The yellow dots (upper panel) show the horizontal coordinates of the boreholes. Vertical cross sections along profiles (b) DD′, (c) EE′, and (d) FF′ of the estimated density-contrast distribution (in color) and the lithological intervals (color ribbons) intersected by boreholes (d1, e1, e2, f1, and f2).

**Fig. 13.** Area 3 — Inversion results using the planting anomalous density inversion. After Carlos et al. (2014). The predicted $g_{zz}$ −component of the gravity gradient tensor by using the inversion is shown by the color map (upper panel). The thick black lines (upper panel) delineate the mapped boundaries of the iron formation according to Dorr (1969). The white lines GG′, HH′, and II′ (upper panel) indicate the locations of the vertical cross sections shown in Figs. 13(b)-(d). The yellow dots and the white triangles (upper panel) show the horizontal coordinates of, respectively, the boreholes and the seeds used in the inversion. Vertical cross sections along profiles (b) GG′, (c) HH′, and (d) II′ of the estimated density-contrast distribution with a single value of 0.75 g/cm³ (in pink) and the lithological intervals (color ribbons) intersected by boreholes (g1 and g2, h1 and h2, i1).

**Fig. 14.** Area 3 — Inversion results using the depth-weighting smoothing inversion. The predicted $g_{zz}$ −component of the gravity gradient tensor by using the inversion is shown by the color map (upper panel). The thick black lines (upper panel) delineate the mapped boundaries of the iron formation according to Dorr (1969). The white lines GG′, HH′, and II′ (upper panel) indicate the locations of the vertical cross sections shown in panels (b)–(d). The yellow dots (upper panel) show the horizontal coordinates of the boreholes. Vertical cross sections along profiles (b) GG′, (c) HH′, and (d) II′ of the estimated density-contrast distribution (in color) and the lithological intervals (color ribbons) intersected by boreholes (g1 and g2, h1 and h2, i1). (For interpretation of the references to color in this figure legend, the reader is referred to the online version of this chapter.)

**Fig. 15.** Perspective view of the estimated density-contrast distribution (in pink) by inverting the six components of the gravity-gradient data shown in Fig. 8. This estimate retrieves the iron-ore body over the southern flank of the Gandarela syncline in Quadrilátero Ferrífero (Brazil).

continuity of the iron-ore body at the neighboring Area 2 in the cross-section FF′ (Figs. 11d and 12d). The lack of estimated iron-ore mass extending itself northwestwards is corroborated by borehole g1 (Figs. 13b and 14b), which does not drill thick masses of the iron formation.

## 5. Which are the geologic characteristics revealed by the inversions?

The planting anomalous density inversion estimates the 3D geometry of the iron-ore body because this inversion allows just two possibilities for the density estimate of each prism: zero or a pre-specified nonnull value (0,75 g/cm$^3$). Besides, this inversion imposes compactness on the solution; hence, the resulting solution will tend to favor compact bodies without holes in its interior as shown Fig. 15 (Carlos et al., 2014). On the contrary, in the depth-weighting smoothing inversion the 3D outline of the iron-ore body is undefined because this method imposes smoothness on the estimated density-contrast distribution. Thus, one cannot define the exact boundary between the iron-ore and the surrounding rocks. In our work, we consider that the large density-contrast estimates indicate the iron-ore body. The estimate from the planting anomalous density inversion contains the outline of the iron-ore body only, disregarding the horizontally adjacent sources. This well-defined boundary of the iron-ore body and its isolation allows calculating not only the iron-ore volume of about 965 million m$^3$, but also the estimated iron-ore mass of about 3 billion metric tons.

Both the planting anomalous density inversion and the depth-weighting smoothing inversion retrieve a variable thickness and width of the estimated iron-ore body along its strike. The planting anomalous density inversion reveals that the thickness and the width of the estimated iron-ore body increase southwestwards, leading to a southwestward increase in the volume of the iron deposit. This predicted large volume of the iron-ore mass may be related to the hinge zone of the Gandarela syncline, which is the zone of maximum compression (Carlos et al., 2014). Because of the smooth character imposed on the solution, the depth-weighting smoothing inversion does not clearly reveal this southwestward increase of the volume of the predicted iron-ore mass,

Both inversions estimate a northeast-elongated iron-ore body which agrees with the geologic mapping accomplished by Dorr (1969). Besides, the estimates of both inversions agree with the information provided by the lithologic logging data of drill holes.

We also note that the estimated iron-ore mass obtained by the depth-weighting smoothing inversion clearly reveals variable dip directions. The estimated iron body dips inwards with respect to the syncline axis in the southernmost portion of the study area, vertically in the central portion, and outwards in the northernmost portion. However, we stress that the depth-weighting smoothing inversion does not retrieves the dip angles of the body. On the other hand, we emphasize that the information about the dip directions of the iron-ore body are merely suggested by the planting anomalous density inversion.

## 6. Conclusions

We have demonstrated the potential of two quite different gravity-gradient inversion methods in revealing different geologic features of an iron-ore deposit. We achieve this by applying the two inversion methods to the gravity gradiometry data of the iron-ore deposit at the southern flank of the Gandarela syncline in Quadrilátero Ferrífero, Brazil. The inversion methods chosen for this study are the depth-weighting smoothing inversion and the planting anomalous density inversion. The depth-weighting smoothing inversion produces a smooth model of the iron-ore mass. This characteristic allows the assessment of the dip directions of the iron-ore body; but it does not allow retrieving its dip angle. Conversely, the planting anomalous density inversion produces a homogeneous and compact model of the iron-ore mass that is concentrated about pre-specified seeds. These characteristics of the planting anomalous density inversion allow the assessment of the predicted total volume and mass the iron ore.

An attractive behavior of applying two quite different gravity-gradient inversion methods is the synergistic effect of their estimates. Important geologic features that are not clearly seen by using one method can show up in the estimate produced by another. This synergistic effect makes feasible to unravel geologic processes that would not be revealed by any one method. One of the geologic processes revealed by the two different estimates in this study is an increase in the volume of the iron-ore mass over the hinge zone of the Gandarela syncline. The large estimated volume of the iron-ore mass followed by the fact that the estimated iron body dips inwards towards the syncline axis, disclosed that the iron-ore deposit is strongly controlled by the Gandarela syncline.

## References

Aster, R.C., Borchers, B., Thurber, C.H., 2013. Parameter estimation and inverse problems. Elsevier Academic Press, Amsterdam, p. 376.

Barbosa, V.C.F., Silva, J.B.C., Medeiros, W.E., 2002. Practical applications of uniqueness theorems in gravimetry: part II — pragmatic incorporation of concrete geologic information. Geophysics 67 (3), 788–794.

Barnes, G., Barraud, J., 2012. Imaging geologic surfaces by inverting gravity gradient data with depth horizons. Geophysics 77, G1–G11.

Carlos, D.U., Uieda, L., Barbosa, V.C.F., 2014. Imaging iron ore from the Quadrilátero Ferrífero (Brazil) using geophysical inversion and drill hole data. Ore Geol. Rev. 61, 268–285.

Dalstra, H.J., 2006. Structural controls of bedded iron ore in the Hamersley Province, Western Australia — an example from the Paraburdoo Ranges. Appl. Earth Sci. (Trans. Inst. Min. Metall. B) 115 (4), 139–145.

Dorr, J.V.N., 1969. Physiographic, stratigraphic and structural development of the Quadrilátero Ferrífero, Minas Gerais, Brazil. U.S. Geol. Surv. Prof. Pap. 641-A, 1–110.

Dransfield, M.H., 2007. Airborne gravity gradiometry in the search for mineral deposits. Proceedings of Exploration 07: Fifth Decennial International Conference on Mineral Exploration, pp. 341–354.

Dransfield, M.H., Christensen, A.N., Diorio, P.A., Rose, M., Stone, P.M., 2001. Falcon test results from the Bathurst Mining Camp. Explor. Geophys. 32, 243–246.

Hagemann, S., Dalstra, H.I., Hodkiewicz, P., Flis, M., Thorne, W., McCuaig, C., 2007. Recent advances in BIF-related iron ore models and exploration strategies. Proceedings of Exploration 07: Fifth Decennial International Conference on Mineral Exploration, pp. 811–821.

Hansen, P., 1992. Analysis of discrete ill-posed problems by means of the L-curve: 69$^{th}$. SIAM Review 34, 561–580.

Li, Y., 2001. 3-D inversion of gravity gradiometer data. 71st Annual International Meeting, SEG, Expanded Abstracts, pp. 1470–1473.

Li, Y., Oldenburg, D.W., 1996. 3-D inversion of magnetic data. Geophysics 61 (2), 394–408.

Martinez, C., Li, Y., Krahenbuhl, R., Braga, M.A., 2013. 3D inversion of airborne gravity gradiometry data in mineral exploration: a case study in the Quadrilátero Ferrífero, Brazil. Geophysics 78, B1–B11.

McLellan, J.G., Oliver, N.H.S., Schaubs, P.M., 2004. Fluid flow in extensional environments; numerical modelling with an application to Hamersley iron ores. J. Struct. Geol. 26, 1157–1171.

Oliveira Jr., V.C., Barbosa, V.C.F., 2013. 3-D radial gravity gradient inversion. Geophys. J. Int. 195, 883–902.

Lane, R., Peljo, M., 2004. Estimating the pre-mining gravity and gravity gradient response of the Broken Hill Ag–Pb–Zn Deposit. ASEG Extended Abstract 2004: 17th Geophysical Conference and Exhibition, pp. 1–5.

Routh, P., Jorgensen, G., Kisabeth, J., 2001. Base of the salt imaging using gravity and tensor gravity data. 72nd Ann. Internat. Mtg., Soc. Expl. Geophys: Expanded Abstracts, pp. 1482–1484.

Silva Dias, F.J.S., Barbosa, V.C.F., Silva, J.B.C., 2009. 3D gravity inversion through an adaptive-learning procedure. Geophysics 74 (3), I9–I21.

Silva, J.B.C., Medeiros, W.E., Barbosa, V.C.F., 2002. Practical applications of uniqueness theorems in gravimetry: part I — constructing sound interpretation methods. Geophysics 67 (3), 788–794.

Uieda, L, Barbosa, V.C.F., 2012. Robust 3D gravity gradient inversion by planting anomalous densities. Geophysics 77 (4), G55–G66.

Zhdanov, M.S., Ellis, R., Mukherjee, S., 2004. Three-dimensional regularized focusing inversion of gravity gradient tensor component data. Geophysics 69, 925–937.